



# Simultaneously enhancing strength and ductility of a high-entropy alloy via gradient hierarchical microstructures

M.N. Hasan<sup>a</sup>, Y.F. Liu<sup>b</sup>, X.H. An<sup>a,\*</sup>, J. Gu<sup>c</sup>, M. Song<sup>c,\*\*</sup>, Y. Cao<sup>b</sup>, Y.S. Li<sup>b</sup>, Y.T. Zhu<sup>b,d</sup>, X.Z. Liao<sup>a,\*\*\*</sup>

<sup>a</sup> School of Aerospace, Mechanical & Mechatronic Engineering, The University of Sydney, Sydney, Australia

<sup>b</sup> Nano and Heterogeneous Materials Center, School of Materials Science and Engineering, Nanjing University of Science and Technology, Nanjing, China

<sup>c</sup> State Key Laboratory of Powder Metallurgy, Central South University, Changsha, China

<sup>d</sup> Department of Materials Science and Engineering, North Carolina State University, Raleigh, United States

## ARTICLE INFO

### Keywords:

High-entropy alloy  
Gradient structure  
Hierarchical nanotwin  
Rotationally accelerated shot peening  
Mechanical properties

## ABSTRACT

Although many high-entropy alloys (HEAs) possess excellent mechanical properties, they are not exempt from the common dilemma of strength–ductility trade-off in most cases, which limits their potential applications. Herein, rotationally accelerated shot peening was used to introduce different gradient hierarchical microstructures, including gradients in twin and dislocation densities, and hierarchical nanotwin, into a CoCrFeNiMn HEA by adjusting the processing parameters. The resulting gradient structures and their effect on hardening behaviour and mechanical properties were systematically explored. Quantitative analysis indicates that deformation twinning, including hierarchical nanotwinning could be more important than dislocation slip in terms of their contribution to hardness and strain hardening capability, depending on the gradient structure profile. It was found that simultaneous improvement of strength and ductility can be achieved in a gradient structure with a thin deformed layer and an undeformed core. Based on our experimental results, we propose that a gradient structure with a largest possible strength difference between the surface layer and the undeformed core would maximize the strength–ductility synergy.

## 1. Introduction

As a new class of metallic materials, high-entropy alloys (HEAs) based on multiple principle elements mixing at near equi-atomic proportions have received considerable attention in the last decade (Cantor et al., 2004; Yeh et al., 2004). Owing to the mixture of multiple elements, HEAs generally possess high configurational entropy, heavy lattice distortion and sluggish diffusion, which enable them to exhibit exceptional structural stability and promising mechanical properties (Yeh, 2013). Excellent combination of strength and ductility in various HEAs have already been reported (Cai et al., 2017; Lee et al., 2018; Shi et al., 2019). Some HEAs also present excellent resistance to fatigue (Tang et al., 2015), creep (Chen et al., 2018), irradiation (Kumar et al., 2016) and corrosion (Chou et al., 2010; Shi et al., 2017). Among various HEAs, the prototypical CoCrFeNiMn HEA, also called the Cantor alloy, exhibits excellent

\* Corresponding author.

\*\* Corresponding author.

\*\*\* Corresponding author.

E-mail addresses: [xianghai.an@sydney.edu.au](mailto:xianghai.an@sydney.edu.au) (X.H. An), [msong@csu.edu.cn](mailto:msong@csu.edu.cn) (M. Song), [xiaozhou.liao@sydney.edu.au](mailto:xiaozhou.liao@sydney.edu.au) (X.Z. Liao).

<https://doi.org/10.1016/j.ijplas.2019.07.017>

Received 3 June 2019; Received in revised form 18 July 2019; Accepted 23 July 2019

Available online 26 July 2019

0749-6419/ © 2019 Elsevier Ltd. All rights reserved.

mechanical properties and maintains its single face-centered cubic (FCC) structure across a wide range of temperatures (Gludovatz et al., 2014; Otto et al., 2013). The easy motion of dislocations and arrest of dislocations at slip bands make essential contributions to the good combination of strength and ductility at room temperature (Lin et al., 2017; Zhang et al., 2015). Especially, lowering the deformation temperature can improve its strength and fracture toughness simultaneously without showing any brittleness due to the transition of the dominant deformation mechanism from dislocation slip to deformation twinning (Gludovatz et al., 2014; Laplanche et al., 2016).

Although the Cantor alloy possesses promising mechanical properties, its yield strength is relatively low at room temperature. Recently, several HEA design strategies were developed to introduce the effects of twinning-induced plasticity (TWIP) (Deng et al., 2015; Ming et al., 2019) and transformation-induced plasticity (TRIP) (Fang et al., 2019; Li et al., 2016), ductile multicomponent intermetallic nanoparticles (Yang et al., 2018) and additives (Brechtel et al., 2019; Niu et al., 2017) into HEAs via tuning their chemical compositions for optimizing their mechanical properties. These methods require elaborate design and control of the chemical composition and processing. Besides, manipulating the microstructure is also an effective way to improve mechanical properties. However, similar to the conventional alloys (An et al., 2019), the HEA also suffers from the strength–ductility trade-off (Bae et al., 2017; Haase and Barrales-Mora, 2018; Kang et al., 2017; Shahmir et al., 2016; Sun et al., 2018), i.e. mutual exclusive relationship between strength and ductility, which seems to be inevitable in materials with homogeneous structures (Lu, 2014).

Recently, various heterogeneous microstructures (Wu and Zhu, 2017), such as heterogeneous lamellae structures (Wu et al., 2015; Zhang et al., 2018) and gradient microstructures (Fang et al., 2011; X. Wu et al., 2014), were specially designed to significantly improve yield strength and at the same time retaining ductility to evade the strength–ductility trade-off (Lu et al., 2019). Gradient structures (GSs, gradation in microstructure from surface to interior) are one of the most well-known heterostructures. Depending on the materials and processing techniques including surface mechanical attrition treatment (SMAT), surface mechanical grinding treatment (SMGT) and pre-torsion, several types of gradient microstructures including gradient nanograins (X. Wu et al., 2014), gradient nanotwins (Wang et al., 2013; Zhu et al., 2019), gradient nanograin/nanotwin (Zhu et al., 2017), and gradient grain/TRIP effect (Chen et al., 2011; Wu et al., 2016) were developed to enhance mechanical properties in various materials including Cu alloys, IF steel, austenitic steel, stainless steels, TWIP steel and Al alloys (Fang et al., 2011; Y. J. Li et al., 2017; Wang et al., 2013; Wei et al., 2014; X. Wu et al., 2014; Zhu et al., 2017). Generally, materials with gradient nanostructures possess high strength without an apparent loss of the ductility. The prominent strength–ductility synergy has been attributed to their heterogeneous deformation mechanisms (Lu, 2014), extra strain hardening (X. Wu et al., 2014), strain partitioning (Wu et al., 2016), back stress (Yang et al., 2016) and synergetic strengthening (X. L. Wu et al., 2014). The most fundamental physics behind the reported synergy is the back-stress strengthening and strain hardening induced by the mechanical incompatibility among heterogeneous domains (Wu and Zhu, 2017).

Although a gradient grain structure was introduced in a cast Cantor alloy using SMAT (Tsai et al., 2018), the effect of this special structure on the mechanical properties is not clear because there may have plenty of cast defects, leading to the low mechanical performance of this as-cast alloy. In addition, the formation of gradient hierarchical structures, the effect of gradient structures on the surface hardening behaviour and the effect of gradient structure profile on the combination of strength and ductility were less understood. Although optimum grain size distribution by an electrodeposition technique on mechanical properties of Ni has been investigated to shed light on optimum GS effect, the process has to be controlled by complicated electrical parameters and is not suitable for practical production of gradient materials (Lin et al., 2018).

In this work, we utilized the rotationally accelerated shot peening (RASP) technique to create different GSs by adjusting the processing parameters and explore the effect of gradient hierarchical structure (gradient twin, dislocation, hierarchical nanotwin) with two different profiles on hardening behaviour and mechanical properties. Microstructural evolution along the depth from sample surface was characterised using advanced electron microscopy. The quantitative contributions of deformation twins and dislocations to the surface hardening induced during RASP were carefully investigated. In addition, the effect of different GSs on the combination of strength and ductility will be discussed and an appropriate GS profile will be suggested for further improvement of strength–ductility synergy of materials.

## 2. Experimental procedures

### 2.1. Material and RASP processing

A Cantor alloy with a nominal composition of  $\text{Cr}_{20}\text{Co}_{20}\text{Fe}_{20}\text{Ni}_{20}\text{Mn}_{20}$  (atomic percentage) was used in this work. The alloy ingots were prepared by arc-melting of a mixture of pure metals (purity > 99.99 wt%) in a Ti-gettered high-purity argon atmosphere. Each ingot was remelted four times to ensure chemical homogeneity. The cast ingots were solution treated at 1473 K for 48 h under a high-purity argon atmosphere. After that, the ingots were cold rolled to sheets with a final thickness of  $\sim 2$  mm and were heat-treated in a vacuum furnace at 1173 K for 2 h to achieve an equiaxed coarse grained (CG) structure. The top and bottom surfaces of samples with dimensions of  $100\text{ mm} \times 100\text{ mm} \times 2\text{ mm}$  were polished for RASP processing to produce a sandwich type of gradient microstructures. Details of the RASP processing technique has been reported in ref (Wang et al., 2017). Samples were processed by RASP at room temperature using similar velocities of  $\sim 70$  m/s for the same duration of 15 min but different ball diameters of 0.5 mm, 1 mm and 2 mm, which are labelled as RASP1, RASP2 and RASP3, respectively.

## 2.2. Mechanical testing and height profile measurements

Following the RASP processing, Vickers microhardness (Hv) was measured to obtain hardness distribution as a function of depth from sample surface, using a Leco Vickers hardness tester (LV700AT) at a depth interval of 25  $\mu\text{m}$  under a load of 0.3 kg with a loading duration time of 15 s. Each hardness value was obtained by averaging at least 8 testing results from the same depth. The error bars for all measured curves was plotted using the standard deviation of all data on each point. Dog-bone shaped tensile specimens with a gauge length of 15 mm, a width of 3 mm and a thickness of 2 mm were cut from RASP-processed samples by electric discharge machining. The uniaxial tensile tests were carried out using an electromechanical testing machine (LFM-20kN) at room temperature and a strain rate of  $10^{-3} \text{ s}^{-1}$ . At least three samples were tested for each RASP processing condition to ensure the reproducibility of stress–strain curves. After tensile experiments, quantitative 3D surface height profiles along the cross-sectional thickness was measured to check the strain gradients imposed by different GS profile using the optical interferometry based profilometer (NanoMap 1000WLI).

## 2.3. Microstructural characterization

Structural characterization was carried out along the depth of the samples using electron back-scattered diffraction (EBSD) technique (Oxford instruments, UK) in a field emission gun scanning electron microscope (SEM) (ZEISS Ultra, Germany). EBSD mapping was performed at an operating voltage of 25 kV with a scanning step size of 100 nm. Back scattered electron (BSE) imaging was taken in the SEM using a retractable BSE detector, while an energy dispersive spectroscopy (EDS) detector attached to the SEM was applied to examine elemental distribution. All samples for EBSD mapping and BSE imaging were prepared by mechanical grinding using 500, 1200 and 4000 SiC grit papers followed by mechanical polishing using diamond suspension with diamond particle sizes of 3  $\mu\text{m}$  and 1  $\mu\text{m}$ . Final polishing was done by the chemico-mechanical polishing technique using aluminium oxide ( $\text{Al}_2\text{O}_3$ ) polishing suspension (OP-AA) with a grain size of 20 nm.

Transmission electron microscopy (TEM) characterisation was performed using a JEOL 3000F microscope operated at 300 kV. TEM specimens taken from specific areas along the depth were identified by EBSD mapping, lifted out using a manipulator, and thinned using focus ion-beam (FIB) (ZEISS Auriga, Germany) to  $\sim 100$  nm thickness with the final milling at a voltage of 10 kV and a current of 10 pA. The specimens were plasma cleaned immediately before TEM experiments. TEM specimens taken from near the center of RASP processed samples were obtained by mechanically polishing to a thickness of  $\sim 35$   $\mu\text{m}$  using 4000 SiC grit papers followed by electropolishing using a Struers Tenupol-5 twin-jet electropolishing unit and a solution of 10% perchloric acid in acetic acid under an applied voltage of 20 V at room temperature. Dislocation densities were calculated by manually counting the numbers of dislocations per unit area from diffraction contrast or high-resolution TEM images.

## 3. Results

### 3.1. Microstructure before RASP processing

The initial microstructure of the CG alloy after cold rolling and annealing consisted of homogeneous equiaxed grains with random crystallographic orientation. Fig. 1(a) shows a typical EBSD inverse pole figure (IPF) map where the black and red lines denote high angle grain boundaries (HAGBs) and twin boundaries (TBs), respectively. The average grain size calculated from IPF maps is around 8  $\mu\text{m}$  which excludes TBs. The SEM image and corresponding EDS composition distribution maps in Fig. 1(b) show that all elements were homogeneously distributed without apparent segregation. The EDS analysis reveals approximately equi-atomic proportions of all elements as shown in Table 1.

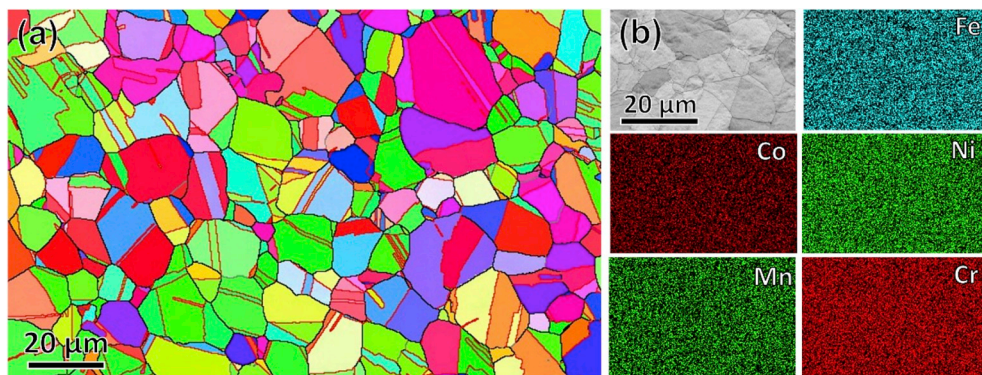


Fig. 1. (a) A typical EBSD IPF map of the alloy with the HAGBs and TBs marked with black and red lines, respectively; and (b) A typical SEM image of the alloy and the distribution of the five elements in the same area.

**Table 1**  
The chemical composition of the alloy measured from EDS.

Elements	Fe	Cr	Co	Ni	Mn
at. %	19.9	20.2	20.1	19.9	19.9

3.2. Effect of RASP parameters on hardness and tensile properties

Fig. 2(a) presents cross-sectional local hardness as a function of the depth of RASP samples from the surface, which reflects the GS profile of the samples. The hardness of the CG alloy is also presented in the figure as a reference. Results show that the local hardness in the surface area was much higher than the internal part of the RASP samples. Both the hardness in the surface area and the hardness gradient were remarkably affected by RASP processing parameters. Larger deformation depth and higher surface hardness were introduced by larger balls because higher impact momentum imposes more severe deformation on samples. The thickness of the deformed layer for RASP1 was approximately 350 μm whereas both RASP2 and RASP3 were deformed across the whole thickness of the samples. While the hardness of the CG alloy was ~1600 MPa, the hardness near the top surface of RASP1, RASP2, and RASP3 samples was ~2800 MPa, 3600 MPa and 3800 MPa, respectively.

Fig. 2(b) exhibits the tensile engineering stress–strain curves of all samples, indicating that the GS profile affects mechanical properties significantly. The yield strength ( $\sigma_{0.2}$ ) was measured to be 323, 418, 560 and 610 MPa with a deviation of  $\pm 5$  MPa from three tests, whereas uniform elongation was 44%, 45%, 17% and 15% for CG, RASP1, RASP2 and RASP3, respectively. Compared to those of CG samples, simultaneous improvement of strength and ductility was achieved only in RASP1 samples. In contrast, both of RASP2 and RASP3 samples showed larger increment of strength but with significantly sacrificed ductility. Although the yield strength of RASP1 was lower than those of RASP2 and RASP3, the ultimate tensile strength of RASP1 was slightly higher than those of RASP2 and RASP3. Moreover, the true ultimate tensile strength of RASP1 exceeded 1000 MPa that was much higher than those of RASP2 and RASP3 due to its larger ductility, as demonstrated by the true stress–strain curves inserted in Fig. 2(c). The strain hardening rate as a function of true strain of all samples is shown in Fig. 2(c). Although no extra strain hardening (X. Wu et al., 2014; Yang et al., 2016, 2015) in the samples with different GSs was observed, RASP1 possessed strain hardening ability similar to that of the CG samples but

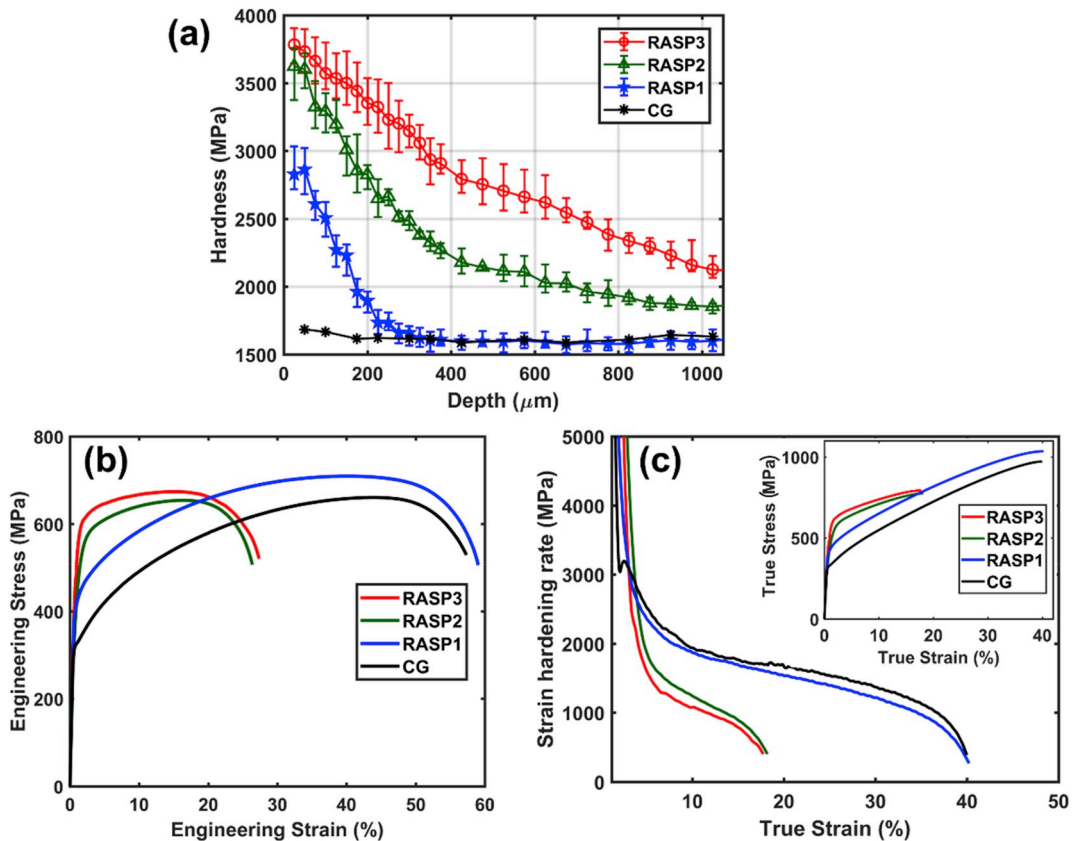


Fig. 2. (a) Hardness distributions along the depth for CG, RASP1, RASP2 and RASP3 samples, (b) Engineering stress–strain curves and (c) strain hardening rate as a function of true strain for CG, RASP1, RASP2 and RASP3 samples. Inset in (c) are true stress–strain curves.

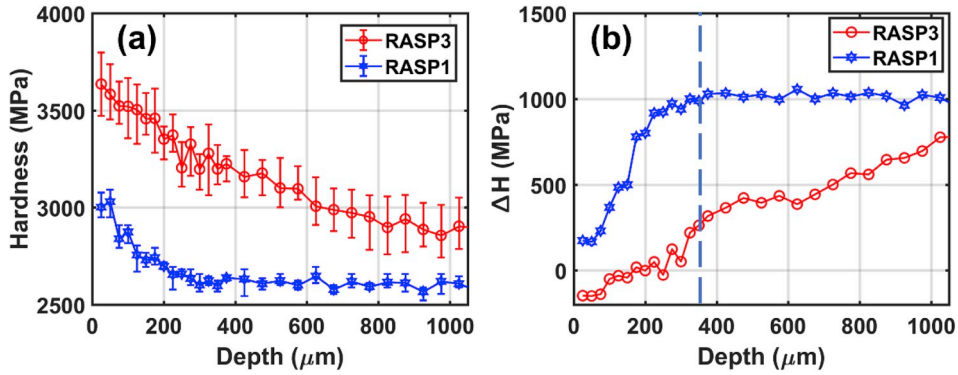


Fig. 3. (a) Microhardness distribution after tensile test and (b) variation of local microhardness before and after tensile test for RASP1 and RASP3 samples.

much better than those of RASP2 and RASP3.

In order to understand the strain hardening behaviour introduced by different GS profiles, the microhardness in the gauge section along cross-sectional thickness (away from the necking part) after tensile failure, was carefully examined. Figs. 3(a) and (b) reveal post-deformation microhardness distribution of RASP1 and RASP3 and their hardness variation ( $\Delta H$ ) before and after tensile test that attributed to the magnitude of retained hardening, respectively. The general shapes of the hardness distribution before (Fig. 2(a)) and after (Fig. 3(a)) tensile tests were similar. However, the  $\Delta H$  distribution for RASP1 was much higher than that for RASP3, as shown in Fig. 3(b), indicating that larger strain hardening was accommodated in RASP1. The  $\Delta H$  of RASP1 increased until the depth of  $\sim 350 \mu\text{m}$  (shown as dotted line in Fig. 3(b)) that was also the thickness of the RASP1 deformed layer and strain gradient should have been induced in this layer during tensile deformation. In contrast,  $\Delta H$  values at the top 200  $\mu\text{m}$  in RASP3 were negative, i.e., the hardness values were slightly decreased after tensile test. This may be attributed to the dynamic recovery because of the high initial density of defects at the top surface introduced by RASP processing (further discussion on dynamic recovery will be given in section 3.4). Those findings suggest that different GS profiles can be achieved by adjusting the RASP processing parameters, which significantly affects the mechanical properties and strain hardening capability of samples.

### 3.3. Microstructures of RASP samples along the depth

As RASP1 and RASP3 possessed two representative GS profiles exhibiting different mechanical properties, the microstructures from the top surface to the depth of  $\sim 200 \mu\text{m}$  in the two samples were characterised by EBSD to examine their gradient structures. Typical cross-sectional IPF, image quality and local misorientation maps for both samples in Fig. 4 reveal the gradient deformation structures along the depth downward. TBs, HAGBs and low angle grain boundaries (LAGBs) are represented by red, black and aqua lines, respectively. For RASP1 samples, the IPF map in Fig. 4(a) shows no obvious change in grain size and the original grain boundaries (GBs) near the top surface were still traceable. Although the grains at the treated surface were not refined, sophisticated

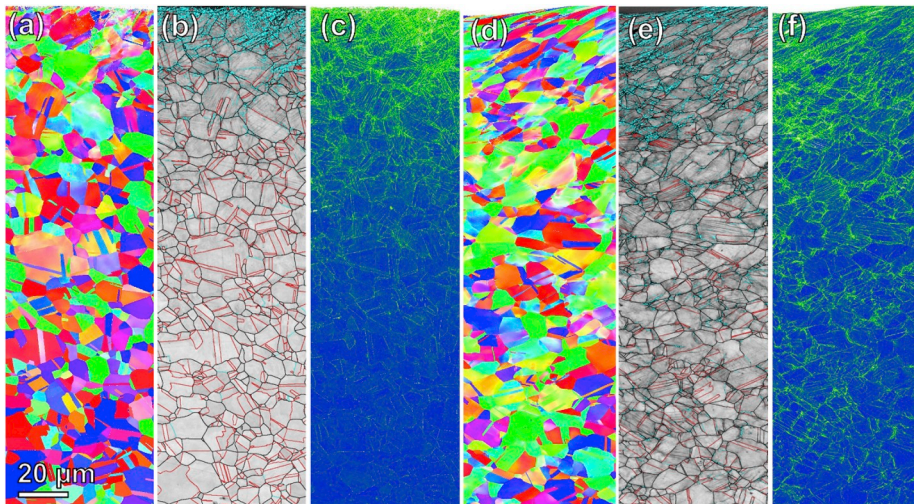
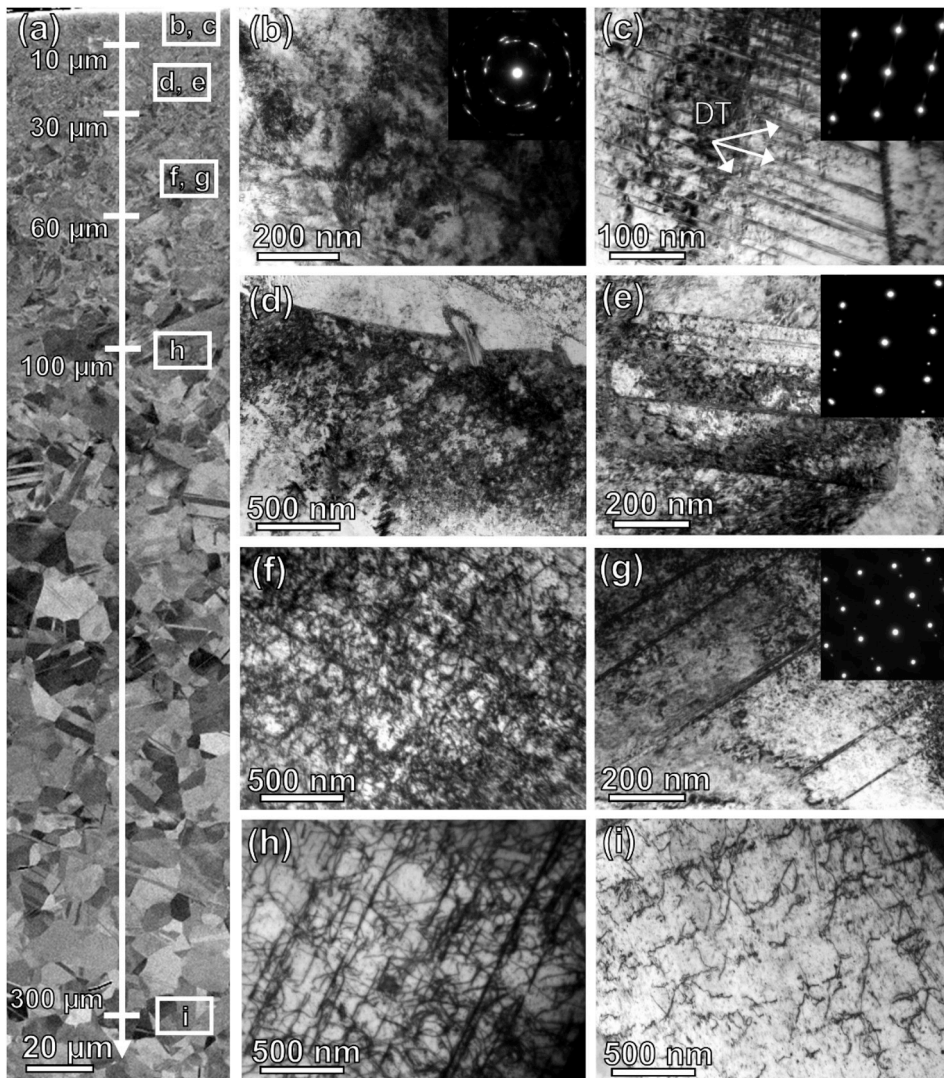


Fig. 4. Typical IPF, image quality and KMP maps showing gradient deformation structure from the surface to  $\sim 200 \mu\text{m}$  depth. (a–c) are for RASP1 samples, and (d–f) are for RASP3 samples.



**Fig. 5.** Microstructures of RASP1 along depths from the surface to  $\sim 320 \mu\text{m}$ . (a) A BSE image showing the overall microstructure. Typical microstructures in areas marked with b, c, ...i are presented by TEM images in (b)–(i), respectively. SAED patterns are inset in some of the TEM images to confirm deformation twin structures.

deformation-induced subgrain structures were clearly discernible. The high density of LAGBs shown in the image quality map in Fig. 4(b) and the large local misorientation illustrated in the Kernel average misorientation (KAM) map in Fig. 4(c) substantiate the severe deformation near the surface. Besides, the image quality map Fig. 4(b) shows some newly formed deformation twins near the top surface, which were not identified by EBSD were confirmed using TEM. The KAM map in Fig. 4(c) shows that intragranular misorientation introduced by geometrically necessary dislocations (GNDs) decreased gradually along the depth and the apparent GND distribution was visible until the depth of  $\sim 100 \mu\text{m}$ . For the RASP3 samples, which were subjected to more severe deformation, there was a very fine-grained layer at the topmost surface, below which the grains were elongated along the plane roughly parallel to the surface within the top layer of  $\sim 40 \mu\text{m}$  as shown in Fig. 4(d–f). Below the region with elongated grains, the grain sizes and shapes were still similar to the original microstructure, while a high density of LAGB and large local misorientation were detected in comparison to those of RASP1 at the similar depth. The change in crystallographic orientation within individual grains and the clear distribution of GNDs continued until  $\sim 200 \mu\text{m}$  in RASP3 samples. Therefore, even though the grains were not refined significantly, hierarchical GSs formed in both samples and was essentially affected by the RASP processing parameters.

Although EBSD observations (Fig. 4) presented overall GS profile, the spatial resolution of EBSD limited its capability of identifying fine microstructures. Therefore, extensive TEM characterisation was carried for RASP1 and RASP3 and the results are presented below. The overall microstructure from the top surface down to the depth of  $\sim 320 \mu\text{m}$  of RASP1 samples is shown by the cross-sectional BSE image in Fig. 5(a). Typical microstructures at the depths marked with b, c, d, ...i in Fig. 6(a) are presented in the TEM images in Fig. 5(b) – 5(i), respectively. The gradient distribution of dislocations and deformation twins was detected along the depth

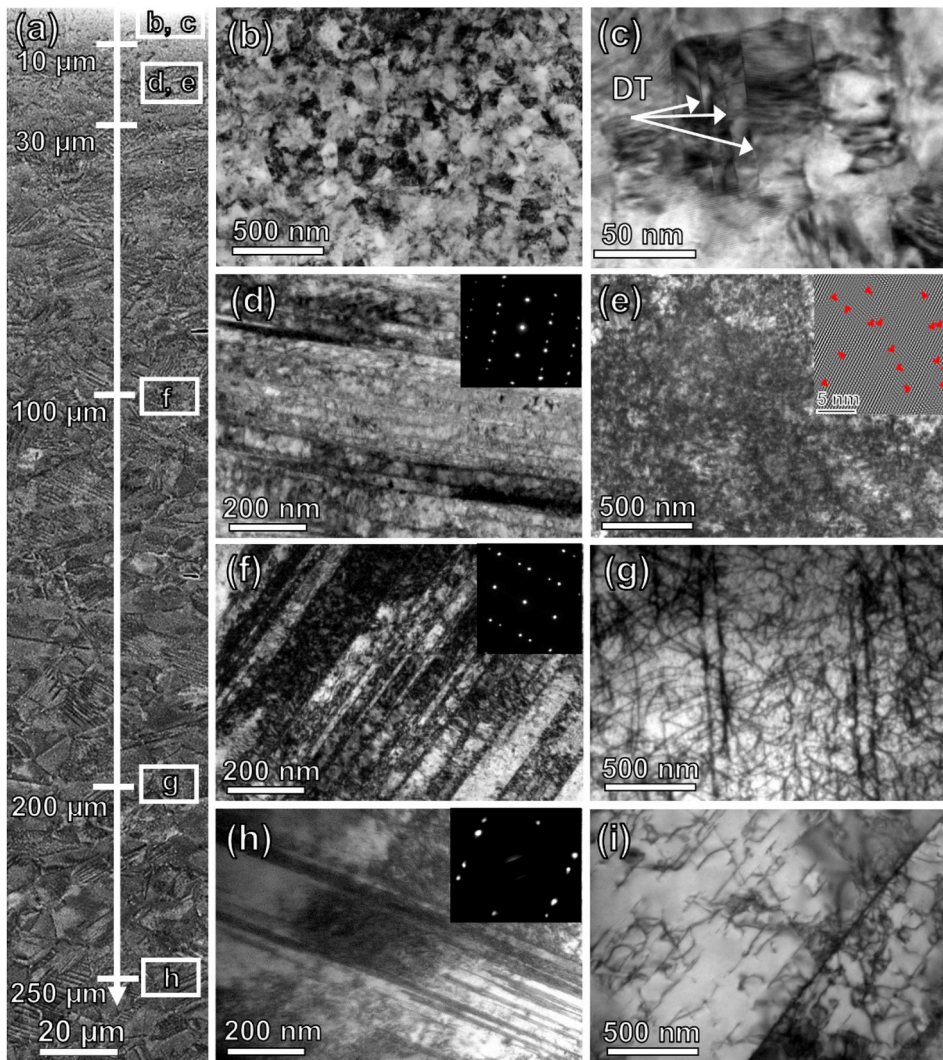


**Fig. 6.** Microstructures of RASP3 along depths from the surface to  $\sim 270 \mu\text{m}$ . (a) A BSE image showing overall microstructure. Typical microstructures in areas marked with b, c, ...and h are presented by TEM images in (b)–(h), respectively. SAED patterns are inset in some of the TEM images, evidencing the existence of twins. Inset in (e) is an HRTEM image with dislocations indicated by red arrows. (i) Planar slip at the center of the sample. (For interpretation of the references to colour in this figure legend, the reader is referred to the Web version of this article.)

of the sample. In the top surface layer with depth of  $< 10 \mu\text{m}$ , profuse dislocation and deformation twins played crucial roles in accommodating the plasticity induced by RASP processing, as shown by Fig. 5(b) and (c). A high density of LAGBs formed due to substantial dislocation activities, evidenced by the selected area diffraction (SAED) pattern inset in Fig. 5(b) in which diffraction spots appeared as arcs because of small angle misorientations from the area that contributed to the SAED pattern. A large number of nano-sized deformation twins (DTs) with average twin width of  $\sim 15 \text{ nm}$  subdivided the original coarse grains into lamellar nanocrystallites (Fig. 5(c)). At the depths of  $10\text{--}30 \mu\text{m}$ , high densities of dislocations near GBs enabled the formation of cell structures (Fig. 5(d)). The density of deformation twins (Fig. 5(e)) was lower than that shown in Fig. 6(c). At the depths of  $30\text{--}60 \mu\text{m}$ , a high density of slip bands was detected (Fig. 5(f)), whereas the amount of deformation twins further decreased (Fig. 5(g)). At the depth of larger than  $60 \mu\text{m}$ , dislocations became the only undertaker of plastic strain. Fig. 5(h) indicates that the deformation mechanism at around  $100 \mu\text{m}$  was governed by planar slip of  $\frac{1}{2}\langle 110 \rangle$  type dislocations gliding along  $\{111\}$  planes similar to that reported at the early stages of deformation of the same alloy in Ref. (Otto et al., 2013). The dislocation activities gradually decreased until  $300 \mu\text{m}$  (Fig. 5(i)), below which the microstructures were similar to those in the CG sample. The microstructural variation along the depth was excellently consistent to the hardness distribution of the gradient sandwiched structure with a CG core in the centre.

A similar cross-sectional BSE image of the overall microstructure of RASP3 from the surface to a depth of  $\sim 270 \mu\text{m}$  is shown in Fig. 6(a). White boxes with labels b, c, ...and h in the figure indicate the depths from which TEM images in Fig. 6(b)–(h), respectively, were obtained. Grains at the topmost surface were substantially refined (Fig. 6(b)) to an average size of  $\sim 110 \text{ nm}$ . Very thin

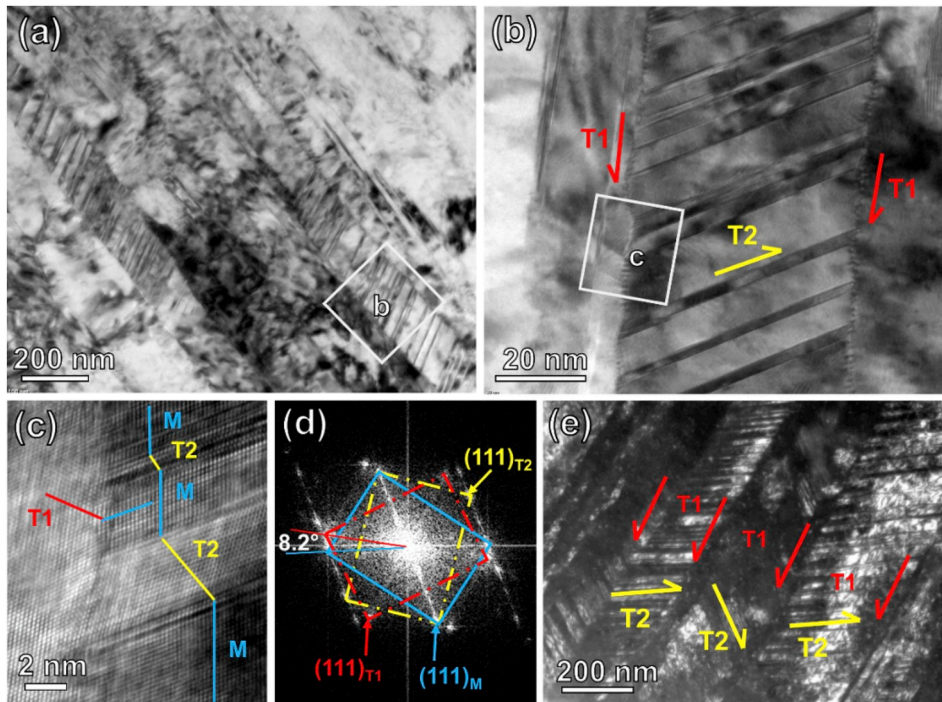


**Fig. 7.** A structure with HNTs near the top surface of RASP3. (a–c) TEM images with magnifications from low to high. The area marked by the white rectangular frame in (a) and (b) is magnified in (b) and (c), respectively. (d) FFT of part of the area shown in (c). Diffraction spots from M, T1 and T2 are indicated using blue, red, and yellow rectangles, respectively. (e) A typical dark-field TEM image of braid-like HNTs. T1 and T2 are indicated using red and yellow arrows, respectively. (For interpretation of the references to colour in this figure legend, the reader is referred to the Web version of this article.)

deformation twins were found in some nano-grains, as exhibited in Fig. 6(c). It is believed that these twins formed via the emissions of Shockley partial dislocations from GBs. These nanostructural features induced by the high-strain-rate impact contributed significant to the high hardness at the topmost surface. The thickness of the nanograined layer was approximately 10  $\mu\text{m}$  from the surface, which is similar to some previous results (Cai et al., 2015; Wang et al., 2013; Xu et al., 2015). In the depths of 10–30  $\mu\text{m}$ , there were profuse deformation twins with an average thickness of  $\sim 20$  nm in many grains as shown in Fig. 6(d). Meanwhile, in some grains whose crystallographic orientation may not be favourable for the activation of deformation twinning, large plastic strain was accommodated by extensive dislocation activities, as shown in Fig. 6(e). Calculated from high-resolution images (an example is shown in the inset in Fig. 6(e)), the estimated dislocation density was as high as  $1.7 \times 10^{15} \text{ m}^{-2}$ . At the depths of 100–200  $\mu\text{m}$ , the density of deformation twins was comparatively lower than that near the surface (Fig. 6(f)), while planar slip was detected (Fig. 6(g)). The volume fraction of deformation twins reduced remarkably at the depth of  $\sim 250$   $\mu\text{m}$  (Fig. 6(h)) but it was still found until 350  $\mu\text{m}$  depth from surface. In line with the hardness distribution of RASP3 (Fig. 2(a)) where the slope of hardness at the top  $\sim 350$   $\mu\text{m}$  was much steeper than that near the center, the twinning behaviour provides apparent hardening due to the nanoscale thicknesses of the twins. Beyond that depth, plastic deformation occurred only by dislocation slip as exhibited in Fig. 6(i).

Due to higher impact energy in RASP3 than in RASP1, two-order HNTs were activated near the surface of 10–30  $\mu\text{m}$ . It can be seen from the TEM images with low to high magnifications in Fig. 7(a–c) that the TBs of primary twins (T1) acted as effective sources and barriers (Cao et al., 2015) for secondary twins (T2), leading to the stair-like bands of T2 confined in T1, which can lead to remarkable hardening. The HRTEM in Fig. 7(c) revealed that the TB is slightly curved, which is usually caused by a high density of dislocations accumulated near the TBs (Cao et al., 2015; Wang et al., 2010). A similar twin structure was recently reported in the same HEA after the dynamic tension test at the strain rate of  $2.2 \times 10^3 \text{ s}^{-1}$  (He et al., 2018) and in Cu–Al alloys and steels with very low stacking fault energies when subjected to SPD (An et al., 2009; Cao et al., 2015). Fig. 7(d) presents the Fast Fourier Transformation (FFT) of Fig. 7(c), showing diffraction spots from T1, T2, and the matrix (M) as marked by red, yellow and blue colour, respectively. It is shown in Fig. 7(d) that there was a slight misorientation of  $8.2^\circ$  between M and T1 due to severe deformation. Similar phenomenon with slight misorientation was observed in TWIP steel and a Cu–Zn alloy after tensile failure (Wang et al., 2010; Wei et al., 2014). Fig. 7(e) shows braid like two-order HNTs where parallel sets of T2 in two orientations were confined by the TBs of T1 that contributed to strengthening. Therefore, these extensive twinning behaviour remarkably refined the microstructure near the top surface of RASP3 samples, leading to much higher hardness in comparison with that of RASP1 samples.

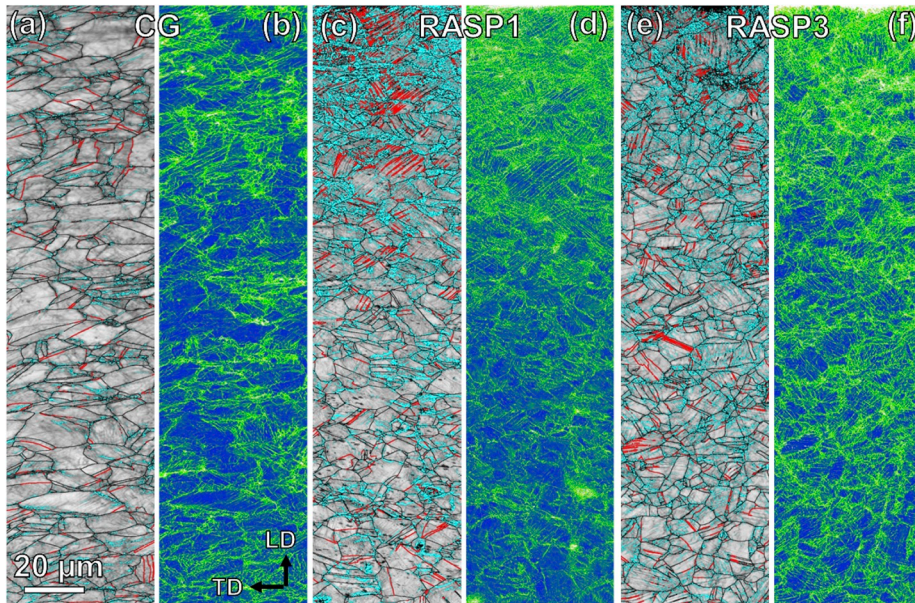


**Fig. 8.** Image quality and KAM maps of the top 200  $\mu\text{m}$  after tensile test for CG (a, b), RASP1 (c, d), and RASP3 (e, f) samples, respectively. TD and LD drawn at the lower right corner of (a) represent the tensile and longitudinal directions, respectively.

### 3.4. Microstructures after tensile deformation

To understand why GS profile has a significant effect on tensile properties and strain hardening behaviour, microstructures after tensile deformation were investigated using EBSD and TEM. Fig. 8 presents the overall microstructures of CG, RASP1 and RASP3 samples after tensile test using image quality and KAM maps. The post-deformation microstructure in the CG samples exhibited slightly elongated grains along the tensile direction (Fig. 8(a)), while there were more dislocations near the GB regions due to dislocation pile-up, leading to higher local misorientation (Fig. 8(b)). Based on the morphology, some TBs marked by red lines in the image quality map in Fig. 8(a) were annealing twins or deformation twins depending on their twin thickness. This will be further discussed based on TEM images in the next section. In contrast, gradient distribution of deformation twins along the depth is clearly visible in both RASP samples as shown in Fig. 8(c) and (e). The density of deformation twins near the top surface was much higher than that of the samples before tensile deformation, implying that extensive twinning events occurred that sustained strain hardening. For the RASP1, high densities of deformation twins formed in the regions from the surface to the depth of  $\sim 60 \mu\text{m}$  (Fig. 8(c)). This depth coincided with that of the sample before tension, above which deformation twins formed during the RASP processing. Although tensile deformation enabled the formation of more deformation twins in the RASP3 (Fig. 8(e)), qualitative evaluation suggests that the increased density of deformation twins was not as obvious as that in RASP1. In addition, based on the KAM maps shown in Fig. 8(d) and (f), the gradient distribution of local misorientation in RASP1 was much more apparent than that in RASP3 and CG. It signals a strain gradient along the depth that could contribute to better combination of mechanical properties in the RASP1 samples.

Fig. 9 presents typical post-tension microstructures of the RASP1 samples near the top surface ((a) – (c) in the upper row) and at the depth of around  $500 \mu\text{m}$  ((d) and (e) in the lower row). In a region near the top surface, two-order HNT structures were activated as shown in Fig. 9(a), where T1 and T2 represent primary and secondary twinning systems, respectively. Similar to the structure in Fig. 9, T2 was always blocked by T1, as shown in Fig. 9(b) and (c). The activation of multiple twinning systems was very effective in storing dislocations and blocking their motion that facilitates the enhancement of both strength and ductility (Zhao et al., 2006). It should be noticed that two-order HNTs were found the surface layer down to the depth of  $\sim 60 \mu\text{m}$ , which was similar to the depth where a single twin system was activated during RASP processing. In regions until  $\sim 60 \mu\text{m}$  from the surface, only a single twin system was found, which was not present before tensile deformation. Thus, HNT systems were activated only in the regions with pre-existing twins. At the depth of  $500 \mu\text{m}$  (the CG core region), the density of deformation twins was very low and dislocation cells with an average cell size of  $\sim 200 \text{nm}$ , which were formed via extensive dislocation activities, dominated the microstructure as exhibited in Fig. 9(d) and (e), respectively. These deformation-induced microstructures at this depth were similar to previous results obtained in the CG samples (Laplanche et al., 2016; Sun et al., 2018).

In contrast, the change of the microstructures after tensile deformation was insignificant in regions near the top surface of RASP3, as shown in Fig. 10(a) and (b). Nanograins in the top surface area and two-order HNTs at the depth of  $\sim 30 \mu\text{m}$  were detected, similar to the microstructures before tensile deformation (see Fig. 6). However, the larger nanograin sizes after tensile deformation (Fig. 10(a)) compared to before tensile deformation (Fig. 6(b)) and the negative hardness profile (Fig. 3(b)) suggested that dynamic recovery occurred during tensile deformation. It has been demonstrated that severe plastic deformation accelerated the formation of

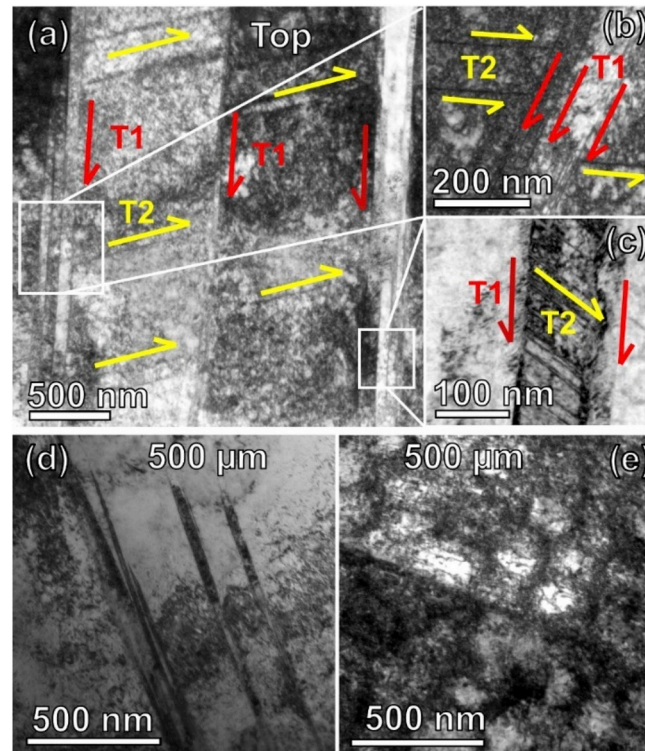


**Fig. 9.** TEM images of the RASP1 after tensile deformation. (a) Two-order HNTs near the top surface. (b) and (c) are magnified images from the areas indicated by the two white square frames in (a), (d) and (e) Low density deformation twins and a dislocation cell structure, respectively, at the depth of  $\sim 500 \mu\text{m}$ .

sub-micrometer sized cell or subgrains via dynamic recovery (Jeong and Kim, 2018). Due to the severe deformation near the top surface by RASP processing, the capability of accommodating further deformation has been nearly run out and this sacrificed the ductility. The TEM images taken from the depth of  $\sim 500 \mu\text{m}$  shown in Fig. 10(c) and (d) indicate the formation of deformation twins and dislocation cells, which were similar to the RASP1 samples at about the same depths. However, in the RASP3 samples, the density of deformation twins was higher and the average size of dislocation cells was  $\sim 100 \text{ nm}$ , which was half of that in the RASP1 samples, indicating that the densities of defects in the structure were nearly saturated. Examination and comparison of the microstructures before and after tensile deformation in terms of HNTs, deformation twins and dislocation sub-structures along the depth suggests that the RASP1 samples exhibited better plasticity and higher capacity for strain hardening to maintain the excellent ductility than RASP3 samples. The severely deformed microstructures in the RASP3 samples, especially in regions near the top surface with nearly saturated defects, restricted further accumulation of crystalline defects, resulting in the apparent loss of ductility.

## 4. Discussion

### 4.1. Effects of RASP on deformation mechanism and hardening behaviour

In the present study, 2-mm thick CG HEA plates were subjected to RASP to introduce different GS profile by changing the RASP processing parameters, which consequently affected their mechanical properties. Since the peening velocity and treatment duration were constants, changing the ball diameter imposed different impact energies to the samples. Previous investigation revealed that the impact energy of SMAT processing, which is determined by the size and velocity of balls and the duration of the processing, is proportional to strain rate and strain which decreases along the depth (Chan et al., 2010). Although the ball sizes used in this study were smaller than those used in SMAT or conventional shot peening, the higher velocity of the balls still enabled larger impact energies. The effect of strain rate and strain on deformation mechanism and how GS influences hardening behaviour is discussed below.

### 4.2. Effect of RASP parameters on deformation mechanism

Dislocation slip and deformation twinning are the two major deformation mechanisms in CG materials and both were observed in the RASP-processed samples. Many factors affect the competition between dislocation slip and deformation twinning. These include applied stress, strain rate, temperature, and grain size (Diao et al., 2017; Zhu et al., 2012). High applied stress that can be achieved by

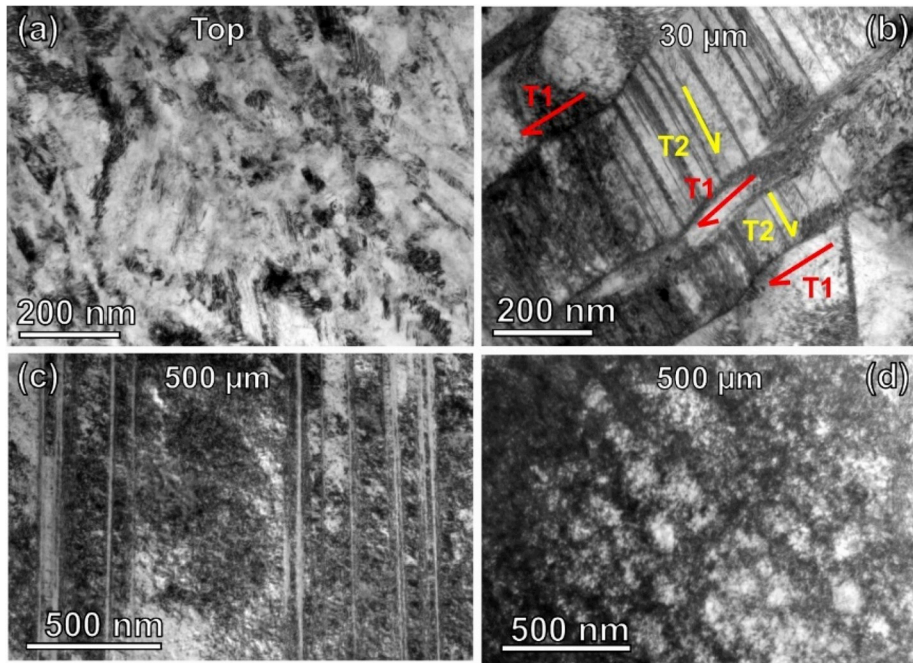


**Fig. 10.** TEM images of a RASP3 sample after tensile deformation. (a) A nano-grained structure in the top surface. (b) A two-order HNT structure at the depth of  $\sim 30 \mu\text{m}$ . (c) Deformation twins and (d) a dislocation cell structure at the depth of  $\sim 500 \mu\text{m}$ .

deformation under constraints (Cao et al., 2012), high strain rate (He et al., 2018), low temperature (Laplanche et al., 2016), and large grain size (Sun et al., 2018) all promote deformation twinning. Indeed, while dislocation slip is the major deformation mode of the CoCrFeMnNi HEA under normal deformation conditions at room temperature, the propensity of deformation twinning in the alloy increases with increasing strain (and therefore applied stress) and/or increasing strain rate.

Because local strain and strain rate imposed by RASP decrease with increasing the depth from the surface of samples, deformation mechanisms are expected to change with the depth. During RASP processing, strain rate has the highest value in the surface layer and decreases rapidly along the depth from the surface. As a result, the propensity of deformation twinning induced by RASP processing decreases along the depth. Indeed, deformation twins were observed only down to the depth of  $\sim 60 \mu\text{m}$  and  $\sim 350 \mu\text{m}$  in RASP1 and RASP3 samples, respectively. Based on a theoretical model (Chan et al., 2010), the strain rate at the depth of  $60 \mu\text{m}$  and  $350 \mu\text{m}$  for the RASP1 and RASP3 samples, respectively, was estimated in the range of  $0.5\text{--}1 \times 10^4$ . The critical twinning stress for the CoCrFeNiMn HEA with an average grain size of  $17 \mu\text{m}$  was measured to be  $720 \pm 30 \text{ MPa}$  (Laplanche et al., 2016). As the average grain size in the present study was only  $8 \mu\text{m}$ , it is reasonable to expect higher critical twinning stress. Indeed, using the hardens values at the depths where twinning disappeared, critical twinning stress was estimated as  $2830/3.0 = 943 \text{ MPa}$  and  $2936/3 = 978 \text{ MPa}$  for RASP1 and RASP3, respectively, where the value of 3 was taken for steel (Hutchings, 2009). The critical twinning stress measured from the two types of samples were reasonably close.

#### 4.3. Hardening behaviour of different GS profile

As mentioned above, both the GS profile and hardness changed with RASP processing parameters. Hardness distribution is affected by GS profile that includes the contribution of deformation twins and dislocation substructures. Both conventional GBs and TBs act as strong barriers to dislocation motion, providing Hall-Petch types of strengthening (Li et al., 2010). Deformation twins formed during deformation offers new TBs that further strengthens the materials through the so called “dynamic Hall-Petch” effect (Otto et al., 2013). Additionally, it is well known that a high density of dislocations is responsible for Taylor hardening (Laplanche et al., 2016). Since no substantial grain refinement occurred except in the topmost surface region of the RASP3 sample, the overall hardness can be approximately expressed as follow based on the microstructural observations:

$$H_v = H_{CG} + H_T + H_p \quad (1)$$

where  $H_{CG}$  is the hardness of the CG HEA, which was  $\sim 1600 \text{ MPa}$ , including the intrinsic hardness of the alloy and conventional GB strengthening,  $H_T$  is the deformation twin induced hardening,  $H_p$  is the Taylor/substructure hardening.  $H_{CG}$  used in this equation is constant because grain size did not change much in both GS samples. The  $H_T$  can be expressed by (Liu et al., 2013; Stepanov et al., 2015):

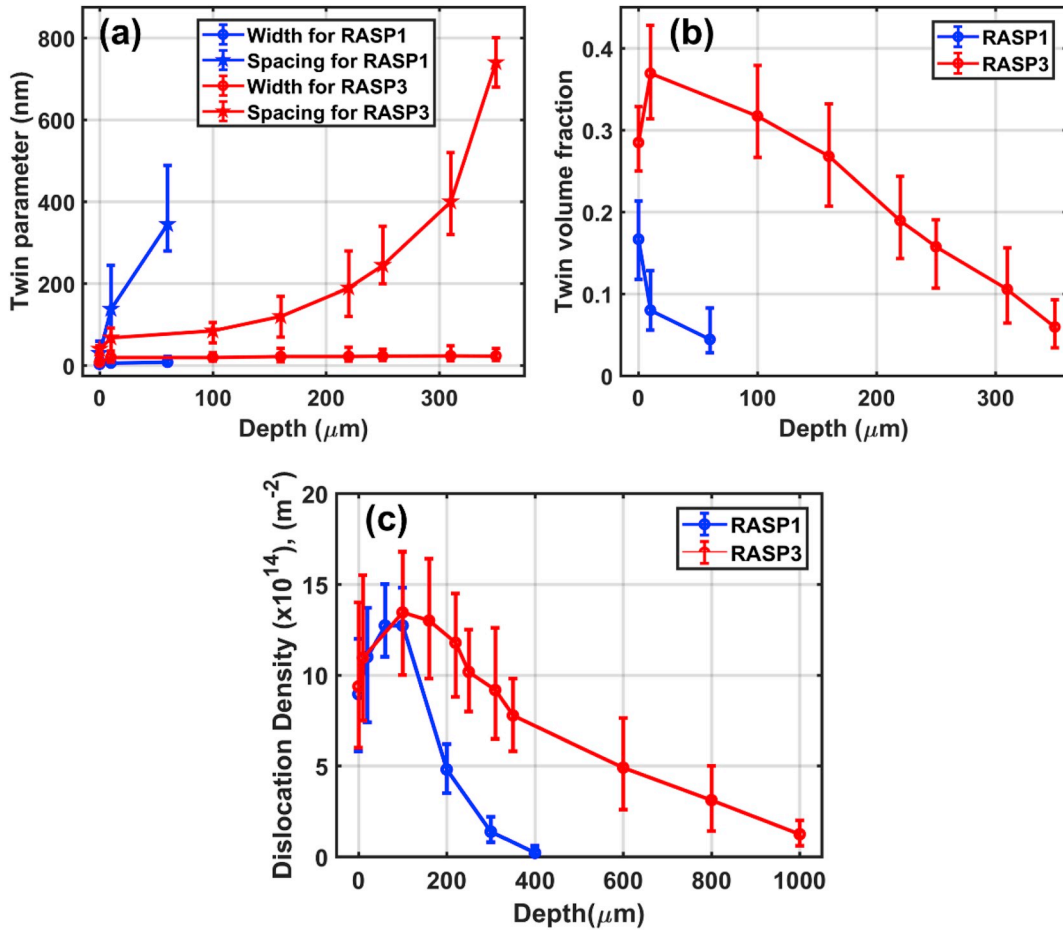


Fig. 11. (a) Twin width and spacing, (b) Twin volume fraction, and (c) dislocation density for both samples along the depth calculated from TEM images.

$$H_T = f \frac{K_y}{\sqrt{t}} \tag{2}$$

where  $f$  is the volume fraction of deformation twins,  $t$  is the average thickness of deformation twins in each GS portion,  $K_y$  is Hall-Petch coefficient also called grain boundary hardening efficiency with the value of  $677 \text{ MPa } \mu\text{m}^{-0.5}$  for the HEA (Liu et al., 2013). Extensive investigations revealed that the thickness of twins can be considered as grain size to calculate Hall-Petch hardening and the slope  $K_y$  for TBs is roughly the same as that for GBs (Kim et al., 2018; Shen et al., 2005; Stepanov et al., 2015). The width and the spacing of deformation twins were measured at each corresponding depth by recourse to the extensive TEM observations. The volume fraction ( $f$ ) of deformation twins can be calculated using the following equation (Laplanche et al., 2016).

$$f = \frac{2t}{\lambda + 2t} \tag{3}$$

where  $\lambda$  is the spacing between twins. The measured average  $\lambda$  and  $t$ , and the calculated  $f$  for both samples along the depth are shown in Fig. 11 (a) and (b). It is clear from Fig. 11 (a) that irrespective of the depth and processing parameters, the width of twins was roughly a constant. However, the spacing of twins increased significantly along the depth and the spacing of twins is much larger in the RASP1 samples than in the RASP3 samples for similar depth values, which implies a higher volume fraction of twins in RASP3 than in RASP1 as shown in Fig. 11(b). Besides the twinning-induced hardening, high densities of dislocations contributed remarkably to the hardening as well, known as the Taylor hardening that can be expressed as (Stepanov et al., 2015):

$$H_p = M\alpha Gb\sqrt{\rho} \tag{4}$$

where the Taylor factor  $M = 3.06$ , a constant  $\alpha = 0.4 \pm 0.1$  for this alloy (Laplanche et al., 2016), shear modulus  $G = 80 \text{ GPa}$  at room temperature, the magnitude of the Burgers vector  $b = 0.258 \text{ nm}$ , and  $\rho$  is the dislocation density. Fig. 11(c) shows the distribution of the dislocations along the depth. In the top surface region, error bars for dislocation density were high due to severe and locally non-uniform deformation that led to inhomogeneous distribution of dislocations. Dislocation densities on both samples

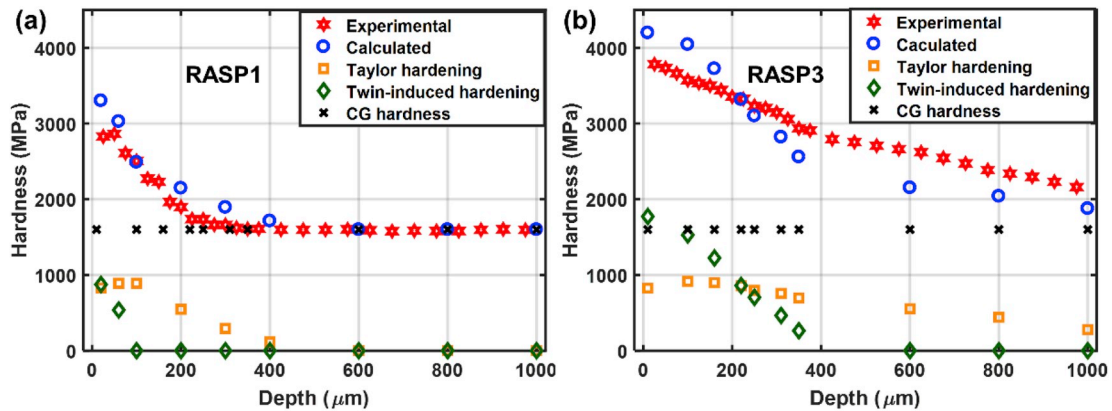


Fig. 12. Hardening contributor from three deformation mechanisms calculated theoretically and compared with experimental values for both samples along the depth.

increased slightly with the depth, which may be a result of the competition between dislocations and deformation twins in accommodating the plasticity (An et al., 2009). Below the depth, the dislocation density decreased apparently for both samples.

Based on the measured and calculated data of the thicknesses and volume fractions of twins, and dislocation densities, the hardening contribution of  $H_T$  and  $H_p$  along the depth can be estimated using equations (2) and (4), as plotted in Fig. 12 for both samples. The overall calculated hardness and the experimental data are included for comparison. It is clear that the calculated data of hardness distribution along the depth match the experimental values very well in the RASP1 samples. Although there were slight difference between the calculated and experimental values in the RASP3 samples that might originate from scattered data in statistics and the more extensive interactions between various deformation mechanisms, the general trend of hardness distribution along the depth is still similar. Therefore, RASP-induced hardening along the depth can be attributed to the variation of deformation twins and dislocations, whose gradient distribution is remarkably affected by the processing parameters.

#### 4.4. Influence of GS profile on tensile properties

It is well known that microstructure plays an essential role in determining the mechanical properties. As shown in Fig. 2(b), tensile properties of the alloy were affected by GS profile and the latter can be manipulated by varying RASP processing parameters. This section will explain the effect of the GS layer on the tensile properties and will discuss the potential to tailor an appropriate GS profile for evading the dilemma of strength–ductility trade-off.

##### 4.4.1. Effect of GS profile on strain gradient

It is well known that strain gradient is an essential characteristic of materials with GSs during tensile deformation (X. Wu et al., 2014). Strain gradient, which can be reflected by the height profile across the thickness direction of a deformed sample, promotes the accumulation of GNDs to induce back stress hardening (J. Y. Li et al., 2017; X. Wu et al., 2014). Fig. 13(a) and (b) show the 3D surface topography measured by optical interferometry, while Fig. 13(c) and (d) exhibit cross-sectional height profiles (total 300 lines) of the RASP1 and RASP3 samples, respectively. The height profiles clearly show that RASP1 exhibited a remarkable height difference of  $> 40 \mu\text{m}$ , whereas RASP3 only presented a height difference of  $\sim 20 \mu\text{m}$ , implying a larger strain gradient in RASP1 than in RASP3. Moreover, the hierarchical twin structure in GS portion of RASP1 samples shown in Fig. 9(a) played a critical role in accommodating plastic deformation, while strain in the CG core was accommodated by dislocation slip, which led to the formation of the dislocation cell structure, and deformation twinning as evidenced in Fig. 9(d) and (e), respectively. Therefore, the uniformly deformed CG core was confined by the non-uniformly deformed GS layer causing mechanical incompatibility. As a result, a complex stress state, i.e., tensile and compressive lateral stress, was produced in the GS layer and the CG core, respectively, activating more slip/twinning systems to enhance defect accumulation and consequently leading to higher strain hardening (X. Wu et al., 2014; Wu et al., 2016). This also produced a strain gradient that induces back stress, which generally formed in heterogeneous or gradient structures, to enhance strain hardening (Wu et al., 2015; Yang et al., 2016). Previous investigations revealed that strain gradient induced in a gradient grain structure causes extra strain hardening to maintain good ductility (X. Wu et al., 2014; X. L. Wu et al., 2014). A recent study on a TWIP steel showed that gradient grain size and GND caused by strain gradient contributed to the simultaneous improvement of ultimate strength and plasticity without improving yield strength (Shao et al., 2018). In contrast, the strain gradient induced in a thin GS profile in this work improved yield strength, tensile strength and ductility. On the other hand, the ductility of the RASP3 samples was apparently reduced because their fully deformed GS provided much smaller strain gradient.

##### 4.4.2. Effects of GS profile on the combination of strength and ductility

In heterostructured materials, yield strength is governed by hard domains, while the ductility is mainly determined by soft domains. The RASP1 samples presented better strength and ductility than the CG samples because (1) the surface layer was much

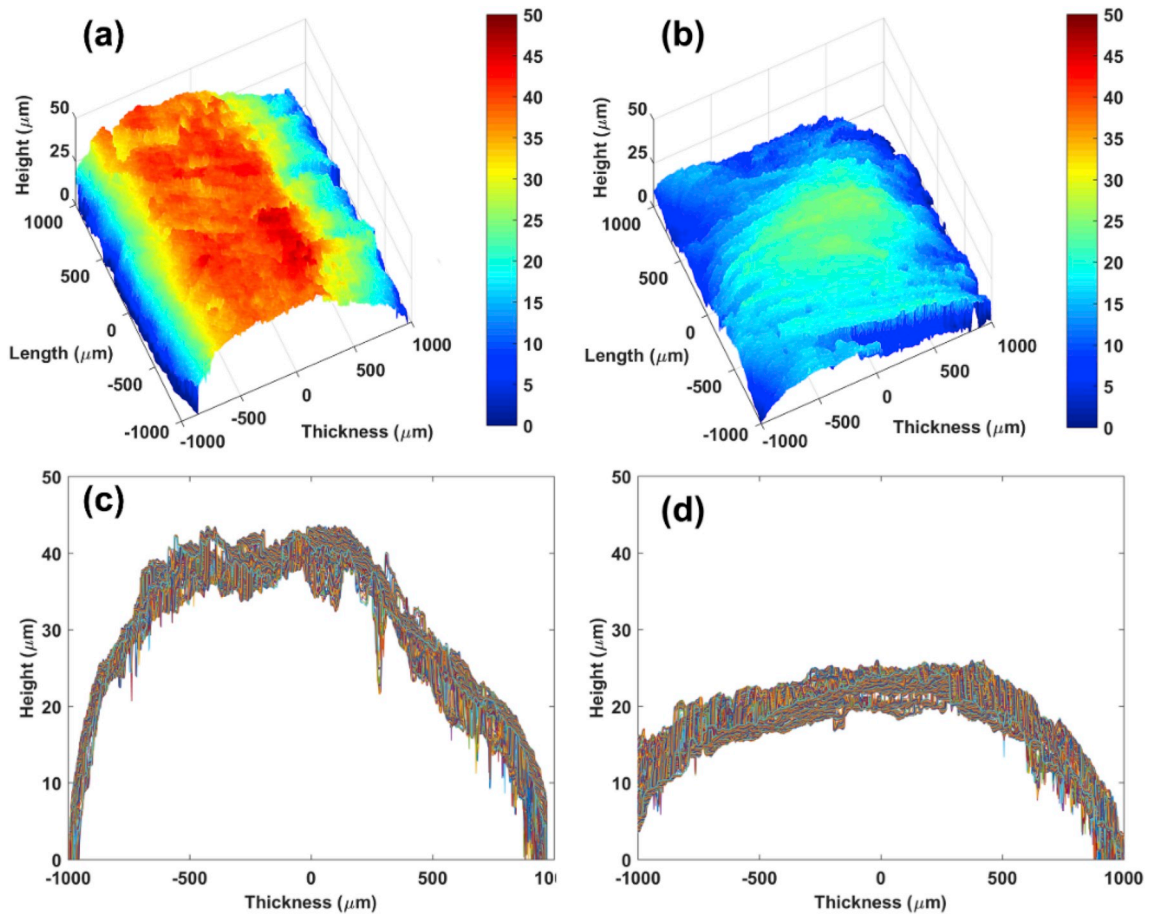


Fig. 13. (a and b) 3D surface topography and (c and d) cross sectional height profiles for RASP1 and RASP3 after tensile deformation.

harder than the CG samples, which provided higher yield strength and (2) the CG core had the same dislocation density as CG samples. The back stress caused by the large strength difference between the hard surface and soft core led to significant pile-up of GNDs that effectively increased the upper limit of allowed dislocation density in the CG core, resulting in a higher work hardening rate. In contrast, the surface layer of the RASP3 samples was very hard, which contributed to their high yield strength. The central part of the RASP3 samples was also deformed/hardened, leading to a high total dislocation density compared to that in the RASP1 samples and a small strain gradient from the surface to the core. The already high dislocation density reduced the space for further increase of dislocation density, resulting in low dislocation hardening capability.

It has been reported that high-order HNT structures can simultaneously improve strength and ductility (Kou et al., 2014). A recent study revealed that a five-order HNT structure in pure Ag can overcome the dilemma of strength–ductility trade-off since this unique microstructure not only impedes dislocation slip for strengthening but also provides nucleation sites of dislocations for sustaining ductility (Liu et al., 2018). In this work, gradient twin structures, which were introduced by RASP processing, generated a HNT structure during the subsequent tensile deformation. However, the HNT structure was not effective for simultaneously enhancing strength and ductility in RASP3. This may be attributed to the fact that the existence of the two-order HNT structure that formed before tensile deformation suppressed the generation of any new high-order HNT structure. Therefore, although the strength of RASP3 was remarkably improved, the loss of ductility was dramatic compared to the CG counterpart. In contrast, the simultaneous improvement of strength and ductility was achieved in the RASP1 samples. The formation of two-order HNT structure until the depth of 60 μm where a single twinning system was activated during RASP played crucial roles in retaining or even increasing strain hardening of RASP1. It was proposed that primary twinning change the crystallographic orientation that would significantly increase the resolved shear stress of another twinning system and therefore trigger secondary twinning, leading to the formation of a HNT structure (Wei et al., 2014). The formation of HNT structure during tensile deformation in the RASP1 sample enhanced the strength by the dynamic Hall-Petch effect in multiple domains and facilitated the twin-twin and dislocation-twin interactions (Alkan et al., 2018; Deng et al., 2015; Ezaz et al., 2011; Wu et al., 2018a,b) to retain or even increase the ductility. Therefore, the RASP and subsequent tensile deformation empowered the activation of various twinning systems enabling simultaneous achievement of high strength, high ductility and excellent strain hardening.

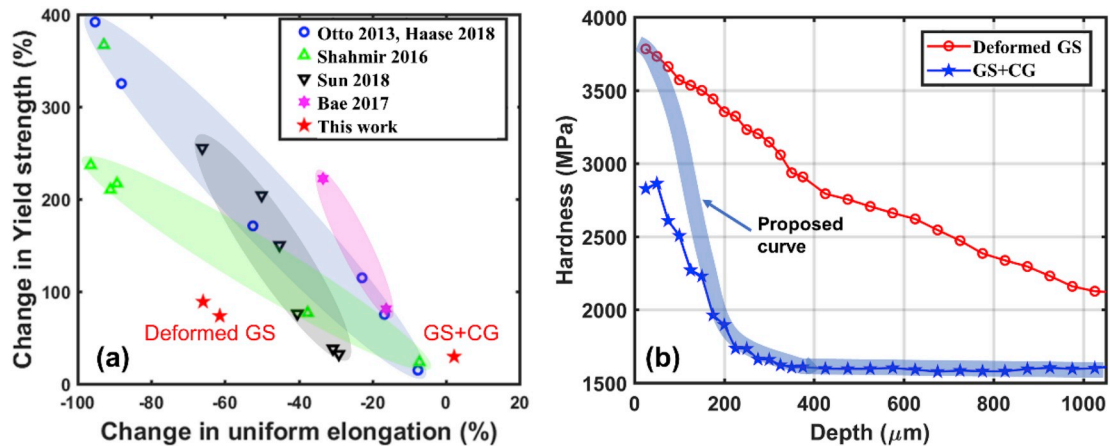


Fig. 14. (a) Relative change (%) in yield strength vs uniform elongation and compared with four references. (b) Replotted hardness distribution of RASP1 and RASP3 and a proposed hardness distribution that would maximize the strength–ductility synergy.

#### 4.5. Optimum GS profile for evading strength–ductility trade-off

Strength–ductility trade-off has been a long-standing dilemma in the materials community. Although HEAs exhibit excellent mechanical properties, they are not exempted from this dilemma (Shahmir et al., 2016). Fig. 14(a) summarizes literature data on how the change in yield strength affected the change in uniform elongation of CG Cantor alloys (Bae et al., 2017; Haase and Barrales-Mora, 2018; Otto et al., 2013; Shahmir et al., 2016; Sun et al., 2018). Data obtained from samples processed using a same method but with different processing parameters are covered with one coloured elliptical shadow in Fig. 14(a). It is clear that all data from the literature presented clear strength–ductility trade-off, i.e., increase in yield strength resulted in loss in ductility. Although RASP2 and RASP3 samples presented the same trend, the RASP1 samples signalled simultaneous improvement of both strength and ductility. Even though the strength increment in the literature data were larger than that of RASP1 in some cases, negative change in uniform elongation would be expected based on the slopes of the ellipses. Therefore, a sandwich structure with a CG core and a thin layer of GS on each side of the surface has clear advantage in improving mechanical properties due to the hierarchical twin structures in the GS layers and prominent strain gradient induced during the subsequent tensile deformation.

While the RASP1 samples presented better strength and ductility than their CG counterparts, their increase in yield strength was not as high as that in the RASP3 samples. To overcome this problem, we propose to acquire a gradient structure that achieves a hardness distribution similar to that shown using the light blue line in Fig. 14(b) in which the hardness distributions of RASP1 and RASP3 are replotted as references. The proposed structure presents a high strength/hardness in the surface layers which is comparable to that of RASP3 so that a high yield strength of the proposed structure could be achieved. On the other hand, the core of the proposed structure remains undeformed so that there is a very large strength difference between the surface layers and the core, which maximizes the back stress hardening capability. Further exploration of sample processing techniques and processing parameters for achieving optimal gradient structures for strength–ductility synergy be carried out in the future (Cheng et al., 2018).

## 5. Conclusions

An equiatomic CrCoFeNiMn HEA was processed by RASP to create different GS profile for the improvement of its mechanical properties. Hardness distribution and tensile mechanical properties of samples with different GS profile were characterized. Various electron microscopic techniques were used for microstructural characterization of samples before and after tensile deformation to understand the formation of GS and the effects of GS on the mechanical properties. The main conclusions are drawn as follow:

- (1) Different gradient hierarchical microstructures can be produced by changing the RASP processing parameters. Typical GS profiles include (i) a thin deformed surface layer with gradient distributions of dislocations and deformation twins and an undeformed core, and (ii) nanograins in the top surface and gradient distributions of dislocations and twins along the thickness down to the core of samples (fully deformed GS).
- (2) While yield strength was almost doubled at the expense of ductility in samples with fully deformed GS profile, simultaneous improvement of strength and ductility was achieved in samples with a thin GS profile. The latter can be attributed to the high strain hardening capability in the undeformed core with thin deformed surface layer.
- (3) The formation of two-order HNTs in the samples with the thin GS profile contributed to the enhancement of strength and ductility due to twin–twin and dislocation–twin interactions. Whereas pre-existing two-order HNTs only improved strength by sacrificing

much of ductility due to its saturation state in the GS profile of a fully deformed structure. Thus an appropriate GS profile is essential for the effectiveness of HNT-induced strength–ductility synergy.

- (4) Strain gradient induced by gradient hierarchical microstructures was much higher in the samples with the thin GS profile than in the samples with fully deformed GS profile. Large strain gradient promotes the accumulation of GNDs in GSs to improve yield strength and sustain the strain hardening. Based on our experimental results, we propose that a GS with a largest possible strength difference between the surface and the undeformed core would maximize the strength–ductility synergy.

## Acknowledgements

The authors appreciate the scientific and technical support from the Australian Microscopy & Microanalysis Research Facility at the University of Sydney. This work was supported by the Australian Research Council under DP190102243 and DE170100053, National Natural Science Foundation of China (grant number 51771229 and 51741106), The University of Sydney under the Robinson Fellowship Scheme and Open Foundation of State Key Laboratory of Powder Metallurgy at Central South University. Liu, Cao and Li were supported by the Jiangsu Key Laboratory of Advanced Micro and Nano Materials.

## References

- Alkan, S., Ojha, A., Sehitoglu, H., 2018. Determination of latent hardening response for FeNiCoCrMn for twin-twin interactions. *Acta Mater.* 147, 149–164. <https://doi.org/10.1016/j.actamat.2017.12.058>.
- An, X., Lin, Q., Qu, S., Yang, G., Wu, S., Zhang, Z.-F., 2009. Influence of stacking-fault energy on the accommodation of severe shear strain in Cu–Al alloys during equal-channel angular pressing. *J. Mater. Res.* 24, 3636–3646. <https://doi.org/10.1557/JMR.2009.0426>.
- An, X.H., Wu, S.D., Wang, Z.G., Zhang, Z.F., 2019. Significance of stacking fault energy in bulk nanostructured materials: insights from Cu and its binary alloys as model systems. *Prog. Mater. Sci.* 101, 1–45. <https://doi.org/10.1016/j.pmatsci.2018.11.001>.
- Bae, J.W., Moon, J., Jang, M.J., Yim, D., Kim, D., Lee, S., Kim, H.S., 2017. Trade-off between tensile property and formability by partial recrystallization of CrMnFeCoNi high-entropy alloy. *Mater. Sci. Eng. A* 703, 324–330. <https://doi.org/10.1016/j.msea.2017.07.079>.
- Brecht, J., Chen, S.Y., Xie, X., Ren, Y., Qiao, J.W., Liaw, P.K., Zinkle, S.J., 2019. Towards a greater understanding of serrated flows in an Al-containing high-entropy-based alloy. *Int. J. Plast.* <https://doi.org/10.1016/j.ijplas.2018.11.011>.
- Cai, B., Liu, B., Kabra, S., Wang, Y., Yan, K., Lee, P.D., Liu, Y., 2017. Deformation mechanisms of Mo alloyed FeCoCrNi high entropy alloy: in situ neutron diffraction. *Acta Mater.* 127, 471–480. <https://doi.org/10.1016/j.actamat.2017.01.034>.
- Cai, B., Ma, X., Moering, J., Zhou, H., Yang, X., Zhu, X., 2015. Enhanced mechanical properties in Cu–Zn alloys with a gradient structure by surface mechanical attrition treatment at cryogenic temperature. *Mater. Sci. Eng. A* 626, 144–149. <https://doi.org/10.1016/j.msea.2014.12.070>.
- Cantor, B., Chang, I.T.H., Knight, P., Vincent, A.J.B., 2004. Microstructural development in equiatomic multicomponent alloys. *Mater. Sci. Eng. A* 375–377, 213–218. <https://doi.org/10.1016/j.msea.2003.10.257>.
- Cao, Y., Wang, Y.B., An, X.H., Liao, X.Z., Kawasaki, M., Ringer, S.P., Langdon, T.G., Zhu, Y.T., 2015. Grain boundary formation by remnant dislocations from the detwinning of thin nano-twins. *Scri. Mater.* 100, 98–101. <https://doi.org/10.1016/j.scriptamat.2015.01.001>.
- Cao, Y., Wang, Y.B., Liao, X.Z., Kawasaki, M., Ringer, S.P., Langdon, T.G., Zhu, Y.T., 2012. Applied stress controls the production of nano-twins in coarse-grained metals. *Appl. Phys. Lett.* 101, 231903. <https://doi.org/10.1063/1.4769216>.
- Chan, H.L., Ruan, H.H., Chen, A.Y., Lu, J., 2010. Optimization of the strain rate to achieve exceptional mechanical properties of 304 stainless steel using high speed ultrasonic surface mechanical attrition treatment. *Acta Mater.* 58, 5086–5096. <https://doi.org/10.1016/j.actamat.2010.05.044>.
- Chen, A.Y., Ruan, H.H., Zhang, J.B., Liu, X.R., Lu, J., 2011. Introducing a hierarchical structure for fabrication of a high performance steel. *Mater. Chem. Phys.* 129, 1096–1103. <https://doi.org/10.1016/j.matchemphys.2011.05.068>.
- Chen, S., Li, W., Xie, X., Brecht, J., Chen, B., Li, P., Zhao, G., Yang, F., Qiao, J., Dahmen, K.A., Liaw, P.K., 2018. Nanoscale serration and creep characteristics of Al<sub>0.5</sub>CoCrCuFeNi high-entropy alloys. *J. Alloy. Comp.* <https://doi.org/10.1016/j.jallcom.2018.04.137>.
- Cheng, Z., Zhou, H., Lu, Q., Gao, H., Lu, L., 2018. Extra strengthening and work hardening in gradient nanotwinned metals. *Science* 80 (362) eaau1925. <https://doi.org/10.1126/science.aau1925>.
- Chou, Y.L., Yeh, J.W., Shih, H.C., 2010. The effect of molybdenum on the corrosion behaviour of the high-entropy alloys Co<sub>1.5</sub>CrFeNi<sub>1.5</sub>Ti<sub>0.5</sub>Mox in aqueous environments. *Corros. Sci.* <https://doi.org/10.1016/j.corsci.2010.04.004>.
- Deng, Y., Tasan, C.C., Pradeep, K.G., Springer, H., Kostka, A., Raabe, D., 2015. Design of a twinning-induced plasticity high entropy alloy. *Acta Mater.* 94, 124–133. <https://doi.org/10.1016/j.actamat.2015.04.014>.
- Diao, H.Y., Feng, R., Dahmen, K.A., Liaw, P.K., 2017. Fundamental deformation behavior in high-entropy alloys: an overview. *Curr. Opin. Solid State Mater. Sci.* 21, 252–266. <https://doi.org/10.1016/j.cossms.2017.08.003>.
- Ezaz, T., Sangid, M.D., Sehitoglu, H., 2011. Energy barriers associated with slip-twin interactions. *Philos. Mag.* <https://doi.org/10.1080/14786435.2010.541166>.
- Fang, Q., Chen, Y., Li, J., Jiang, C., Liu, B., Liu, Y., Liaw, P.K., 2019. Probing the phase transformation and dislocation evolution in dual-phase high-entropy alloys. *Int. J. Plast.* 114, 161–173. <https://doi.org/10.1016/j.ijplas.2018.10.014>.
- Fang, T.H., Li, W.L., Tao, N.R., Lu, K., 2011. Revealing extraordinary intrinsic tensile plasticity in gradient nano-grained copper. *Science* 80 (331), 1587–1590. <https://doi.org/10.1126/science.1200177>.
- Gludovatz, B., Hohenwarter, A., Catoor, D., Chang, E.H., George, E.P., Ritchie, R.O., 2014. A fracture-resistant high-entropy alloy for cryogenic applications. *Science* 80 (345), 1153–1158. <https://doi.org/10.1126/science.1254581>.
- Haase, C., Barrales-Mora, L.A., 2018. Influence of deformation and annealing twinning on the microstructure and texture evolution of face-centered cubic high-entropy alloys. *Acta Mater.* 150, 88–103. <https://doi.org/10.1016/j.actamat.2018.02.048>.
- He, J., Wang, Q., Zhang, H., Dai, L., Mukai, T., Wu, Y., Liu, X., Wang, H., Nieh, T.-G., Lu, Z., 2018. Dynamic deformation behavior of a face-centered cubic FeCoNiCrMn high-entropy alloy. *Sci. Bull.* 63, 362–368. <https://doi.org/10.1016/j.scib.2018.01.022>.
- Hutchings, I.M., 2009. The contributions of David Tabor to the science of indentation hardness. *J. Mater. Res.* 24, 581–589. <https://doi.org/10.1557/jmr.2009.0085>.
- Jeong, H.T., Kim, W.J., 2018. Microstructures and mechanical properties of the non-equiatomic FeMnNiCoCr high entropy alloy processed by differential speed rolling. *Mater. Sci. Eng. A*. <https://doi.org/10.1016/j.msea.2018.04.106>.
- Kang, M., Won, J.W., Kwon, J.B., Na, Y.S., 2017. Intermediate strain rate deformation behavior of a CoCrFeMnNi high-entropy alloy. *Mater. Sci. Eng. A* 707, 16–21. <https://doi.org/10.1016/j.msea.2017.09.026>.
- Kim, J.H., Lim, K.R., Won, J.W., Na, Y.S., Kim, H.S., 2018. Mechanical properties and deformation twinning behavior of as-cast CoCrFeMnNi high-entropy alloy at low and high temperatures. *Mater. Sci. Eng. A* 712, 108–113. <https://doi.org/10.1016/j.msea.2017.11.081>.
- Kou, H., Lu, J., Li, Y., 2014. High-strength and high-ductility nanostructured and amorphous metallic materials. *Adv. Mater.* 26, 5518–5524. <https://doi.org/10.1002/adma.201401595>.
- Kumar, N.A.P.K., Li, C., Leonard, K.J., Bei, H., Zinkle, S.J., 2016. Microstructural stability and mechanical behavior of FeNiMnCr high entropy alloy under ion irradiation. *Acta Mater.* <https://doi.org/10.1016/j.actamat.2016.05.007>.

- Laplanche, G., Kostka, A., Horst, O.M., Eggeler, G., George, E.P., 2016. Microstructure evolution and critical stress for twinning in the CrMnFeCoNi high-entropy alloy. *Acta Mater.* 118, 152–163. <https://doi.org/10.1016/j.actamat.2016.07.038>.
- Lee, C., Song, G., Gao, M.C., Feng, R., Chen, P., Brechtel, J., Chen, Y., An, K., Guo, W., Poplawsky, J.D., Li, S., Samaei, A.T., Chen, W., Hu, A., Choo, H., Liaw, P.K., 2018. Lattice distortion in a strong and ductile refractory high-entropy alloy. *Acta Mater.* 160, 158–172. <https://doi.org/10.1016/j.actamat.2018.08.053>.
- Li, J., Weng, G.J., Chen, S., Wu, X., 2017. On strain hardening mechanism in gradient nanostructures. *Int. J. Plast.* 88, 89–107. <https://doi.org/10.1016/j.ijplas.2016.10.003>.
- Li, X., Wei, Y., Lu, L., Lu, K., Gao, H., 2010. Dislocation nucleation governed softening and maximum strength in nano-twinned metals. *Nature* 464, 877–880. <https://doi.org/10.1038/nature08929>.
- Li, Y., Li, L., Nie, J., Cao, Y., Zhao, Y., Zhu, Y., 2017. Microstructural evolution and mechanical properties of a 5052 Al alloy with gradient structures. *J. Mater. Res.* 32, 4443–4451. <https://doi.org/10.1557/jmr.2017.310>.
- Li, Z., Pradeep, K.G., Deng, Y., Raabe, D., Tasan, C.C., 2016. Metastable high-entropy dual-phase alloys overcome the strength-ductility trade-off. *Nature* 534, 227–230. <https://doi.org/10.1038/nature17981>.
- Lin, Q., An, X., Liu, H., Tang, Q., Dai, P., Liao, X., 2017. In-situ high-resolution transmission electron microscopy investigation of grain boundary dislocation activities in a nanocrystalline CrMnFeCoNi high-entropy alloy. *J. Alloy. Comp.* 709, 802–807. <https://doi.org/10.1016/j.jallcom.2017.03.194>.
- Lin, Y., Pan, J., Zhou, H.F., Gao, H.J., Li, Y., 2018. Mechanical properties and optimal grain size distribution profile of gradient grained nickel. *Acta Mater.* 153, 279–289. <https://doi.org/10.1016/j.actamat.2018.04.065>.
- Liu, W.H., Wu, Y., He, J.Y., Nieh, T.G., Lu, Z.P., 2013. Grain growth and the Hall-Petch relationship in a high-entropy FeCrNiCoMn alloy. *Scr. Mater.* 68, 526–529. <https://doi.org/10.1016/j.scriptamat.2012.12.002>.
- Liu, X., Sun, L., Zhu, L., Liu, J., Lu, K., Lu, J., 2018. High-order hierarchical nanotwins with superior strength and ductility. *Acta Mater.* 149, 397–406. <https://doi.org/10.1016/j.actamat.2018.01.047>.
- Lu, K., 2014. Making strong nanomaterials ductile with gradients. *Science* 80 (345), 1455–1456. <https://doi.org/10.1126/science.1255940>.
- Lu, X., Zhang, X., Shi, M., Roters, F., Kang, G., Raabe, D., 2019. Dislocation mechanism based size-dependent crystal plasticity modeling and simulation of gradient nano-grained copper. *Int. J. Plast.* 113, 52–73. <https://doi.org/10.1016/j.ijplas.2018.09.007>.
- Ming, K., Bi, X., Wang, J., 2019. Strength and ductility of CrFeCoNiMo alloy with hierarchical microstructures. *Int. J. Plast.* 113, 255–268. <https://doi.org/10.1016/j.ijplas.2018.10.005>.
- Niu, S., Kou, H., Zhang, Y., Wang, J., Li, J., 2017. The characteristics of serration in Al<sub>0.5</sub>CoCrFeNi high entropy alloy. *Mater. Sci. Eng. A*. <https://doi.org/10.1016/j.msea.2017.05.075>.
- Otto, F., Dlouhý, A., Somsen, C., Bei, H., Eggeler, G., George, E.P., 2013. The influences of temperature and microstructure on the tensile properties of a CoCrFeMnNi high-entropy alloy. *Acta Mater.* 61, 5743–5755. <https://doi.org/10.1016/j.actamat.2013.06.018>.
- Shahmir, H., He, J., Lu, Z., Kawasaki, M., Langdon, T.G., 2016. Effect of annealing on mechanical properties of a nanocrystalline CoCrFeNiMn high-entropy alloy processed by high-pressure torsion. *Mater. Sci. Eng. A* 676, 294–303. <https://doi.org/10.1016/j.msea.2016.08.118>.
- Shao, C.W., Zhang, P., Zhu, Y.K., Zhang, Z.J., Tian, Y.Z., Zhang, Z.F., 2018. Simultaneous improvement of strength and plasticity: additional work-hardening from gradient microstructure. *Acta Mater.* 145, 413–428. <https://doi.org/10.1016/j.actamat.2017.12.028>.
- Shen, Y.F., Lu, L., Lu, Q.H., Jin, Z.H., Lu, K., 2005. Tensile properties of copper with nano-scale twins. *Scr. Mater.* 52, 989–994. <https://doi.org/10.1016/j.scriptamat.2005.01.033>.
- Shi, P., Ren, W., Zheng, T., Ren, Z., Hou, X., Peng, J., Hu, P., Gao, Y., Zhong, Y., Liaw, P.K., 2019. Enhanced strength–ductility synergy in ultrafine-grained eutectic high-entropy alloys by inheriting microstructural lamellae. *Nat. Commun.* <https://doi.org/10.1038/s41467-019-08460-2>.
- Shi, Y., Yang, B., Xie, X., Brechtel, J., Dahmen, K.A., Liaw, P.K., 2017. Corrosion of Al x CoCrFeNi high-entropy alloys: Al-content and potential scan-rate dependent pitting behavior. *Corros. Sci.* <https://doi.org/10.1016/j.corsci.2017.02.019>.
- Stepanov, N., Tikhonovsky, M., Yurchenko, N., Zybakin, D., Klimova, M., Zherebtsov, S., Efimov, A., Salishchev, G., 2015. Effect of cryo-deformation on structure and properties of CoCrFeNiMn high-entropy alloy. *Intermetallics* 59, 8–17. <https://doi.org/10.1016/j.intermet.2014.12.004>.
- Sun, S.J., Tian, Y.Z., Lin, H.R., Yang, H.J., Dong, X.G., Wang, Y.H., Zhang, Z.F., 2018. Transition of twinning behavior in CoCrFeMnNi high entropy alloy with grain refinement. *Mater. Sci. Eng. A* 712, 603–607. <https://doi.org/10.1016/j.msea.2017.12.022>.
- Tang, Z., Yuan, T., Tsai, C.W., Yeh, J.W., Lundin, C.D., Liaw, P.K., 2015. Fatigue behavior of a wrought Al<sub>0.5</sub>CoCrCuFeNi two-phase high-entropy alloy. *Acta Mater.* <https://doi.org/10.1016/j.actamat.2015.07.004>.
- Tsai, M.T., Huang, J.C., Tsai, W.Y., Chou, T.H., Chen, C.-F., Li, T.H., Jang, J.S.C., 2018. Effects of ultrasonic surface mechanical attrition treatment on microstructures and mechanical properties of high entropy alloys. *Intermetallics* 93, 113–121. <https://doi.org/10.1016/j.intermet.2017.11.018>.
- Wang, H.T., Tao, N.R., Lu, K., 2013. Architected surface layer with a gradient nanotwinned structure in a Fe–Mn austenitic steel. *Scr. Mater.* 68, 22–27. <https://doi.org/10.1016/j.scriptamat.2012.05.041>.
- Wang, X., Li, Y.S., Zhang, Q., Zhao, Y.H., Zhu, Y.T., 2017. Gradient structured copper by rotationally accelerated shot peening. *J. Mater. Sci. Technol.* 33, 758–761. <https://doi.org/10.1016/j.jmst.2016.11.006>.
- Wang, Y.B., Liao, X.Z., Zhao, Y.H., Lavernia, E.J., Ringer, S.P., Horita, Z., Langdon, T.G., Zhu, Y.T., 2010. The role of stacking faults and twin boundaries in grain refinement of a Cu–Zn alloy processed by high-pressure torsion. *Mater. Sci. Eng. A* 527, 4959–4966. <https://doi.org/10.1016/j.msea.2010.04.036>.
- Wei, Y., Li, Y., Zhu, L., Liu, Y., Lei, X., Wang, G., Wu, Y., Mi, Z., Liu, J., Wang, H., Gao, H., 2014. Evading the strength–ductility trade-off dilemma in steel through gradient hierarchical nanotwins. *Nat. Commun.* 5, 3580. <https://doi.org/10.1038/ncomms4580>.
- Wu, X., Jiang, P., Chen, L., Yuan, F., Zhu, Y.T., 2014. Extraordinary strain hardening by gradient structure. *Proc. Natl. Acad. Sci.* 111, 7197–7201. <https://doi.org/10.1073/pnas.1324069111>.
- Wu, X., Yang, M., Yuan, F., Wu, G., Wei, Y., Huang, X., Zhu, Y., 2015. Heterogeneous lamella structure unites ultrafine-grain strength with coarse-grain ductility. *Proc. Natl. Acad. Sci.* 112, 14501–14505. <https://doi.org/10.1073/pnas.1517193112>.
- Wu, X., Zhu, Y., 2017. Heterogeneous materials: a new class of materials with unprecedented mechanical properties. *Mater. Res. Lett.* 5, 527–532. <https://doi.org/10.1080/21663831.2017.1343208>.
- Wu, X.L., Jiang, P., Chen, L., Zhang, J.F., Yuan, F.P., Zhu, Y.T., 2014. Synergetic strengthening by gradient structure. *Mater. Res. Lett.* 2, 185–191. <https://doi.org/10.1080/21663831.2014.935821>.
- Wu, X.L., Yang, M.X., Yuan, F.P., Chen, L., Zhu, Y.T., 2016. Combining gradient structure and TRIP effect to produce austenite stainless steel with high strength and ductility. *Acta Mater.* 112, 337–346. <https://doi.org/10.1016/j.actamat.2016.04.045>.
- Wu, Y., Bönisch, M., Alkan, S., Abuzaid, W., Sehitoglu, H., 2018a. Experimental determination of latent hardening coefficients in FeMnNiCoCr. *Int. J. Plast.* 105, 239–260. <https://doi.org/10.1016/j.ijplas.2018.02.016>.
- Wu, Y., Sehitoglu, H., B., M., 2018b. Acta Materialia Hardening by slip-twin and twin-twin interactions in FeMnNiCoCr 153, 391–403. <https://doi.org/10.1016/j.actamat.2018.04.054>.
- Xu, P., Luo, H., Han, Z., Zou, J., 2015. Tailoring a gradient nanostructured age-hardened aluminum alloy using high-gradient strain and strain rate. *Mater. Des.* 85, 240–247. <https://doi.org/10.1016/j.matdes.2015.07.009>.
- Yang, M., Pan, Y., Yuan, F., Zhu, Y., Wu, X., 2016. Back stress strengthening and strain hardening in gradient structure. *Mater. Res. Lett.* 4, 145–151. <https://doi.org/10.1080/21663831.2016.1153004>.
- Yang, T., Zhao, Y.L., Tong, Y., Jiao, Z.B., Wei, J., Cai, J.X., Han, X.D., Chen, D., Hu, A., Kai, J.J., Lu, K., Liu, Y., Liu, C.T., 2018. Multicomponent intermetallic nanoparticles and superb mechanical behaviors of complex alloys. *Science* 80 (362), 933–937. <https://doi.org/10.1126/science.aas8815>.
- Yang, X., Ma, X., Moering, J., Zhou, H., Wang, W., Gong, Y., Tao, J., Zhu, Y., Zhu, X., 2015. Influence of gradient structure volume fraction on the mechanical properties of pure copper. *Mater. Sci. Eng. A* 645, 280–285. <https://doi.org/10.1016/j.msea.2015.08.037>.
- Yeh, J.-W., 2013. Alloy design strategies and future trends in high-entropy alloys. *JOM* 65, 1759–1771. <https://doi.org/10.1007/s11837-013-0761-6>.
- Yeh, J.-W., Chen, S.-K., Lin, S.-J., Gan, J.-Y., Chin, T.-S., Shun, T.-T., Tsau, C.-H., Chang, S.-Y., 2004. Nanostructured high-entropy alloys with multiple principal

- elements: novel alloy design concepts and outcomes. *Adv. Eng. Mater.* 6, 299–303. <https://doi.org/10.1002/adem.200300567>.
- Zhang, C., Zhu, C., Harrington, T., Vecchio, K., 2018. Design of non-equiaxed high entropy alloys with heterogeneous lamella structure towards strength-ductility synergy. *Scr. Mater.* 154, 78–82. <https://doi.org/10.1016/j.scriptamat.2018.05.020>.
- Zhang, Z.J., Mao, M.M., Wang, J., Gludovatz, B., Zhang, Z., Mao, S.X., George, E.P., Yu, Q., Ritchie, R.O., 2015. Nanoscale origins of the damage tolerance of the high-entropy alloy CrMnFeCoNi. *Nat. Commun.* 6, 2–7. <https://doi.org/10.1038/ncomms10143>.
- Zhao, Y.H., Liao, X.Z., Cheng, S., Ma, E., Zhu, Y.T., 2006. Simultaneously increasing the ductility and strength of nanostructured alloys. *Adv. Mater.* 18, 2280–2283. <https://doi.org/10.1002/adma.200600310>.
- Zhu, L., Ruan, H., Chen, A., Guo, X., Lu, J., 2017. Microstructures-based constitutive analysis for mechanical properties of gradient-nanostructured 304 stainless steels. *Acta Mater.* 128, 375–390. <https://doi.org/10.1016/j.actamat.2017.02.035>.
- Zhu, L., Wen, C., Gao, C., Guo, X., Chen, Z., Lu, J., 2019. Static and dynamic mechanical behaviors of gradient-nanotwinned stainless steel with a composite structure: experiments and modeling. *Int. J. Plast.* 114, 272–288. <https://doi.org/10.1016/j.ijplas.2018.11.005>.
- Zhu, Y.T., Liao, X.Z., Wu, X.L., 2012. Deformation twinning in nanocrystalline materials. *Prog. Mater. Sci.* 57, 1–62. <https://doi.org/10.1016/j.pmatsci.2011.05.001>.